Journal of Physics:
Complexity

Bifurcation behavior of the coupled SPG-AMOC system

To cite this article: Jonas Thies and Henk A Dijkstra 2026 *J. Phys. Complex.* **7** 015011

Journal of Physics: Complexity

OPEN ACCESS

RECEIVED
2 August 2025

REVISED
25 February 2026

ACCEPTED FOR PUBLICATION
10 March 2026

PUBLISHED
20 March 2026

PAPER

Bifurcation behavior of the coupled SPG-AMOC system

Jonas Thies[1] and **Henk A Dijkstra**[2,*]

[1] Delft Institute of Applied Mathematics, Faculty of Electrical Engineering, Mathematics and Computer Science, Delft University of Technology, Delft, The Netherlands
[2] Institute for Marine and Atmospheric research Utrecht &, Center for Complex System Studies, Department of Physics, Utrecht University, Utrecht, The Netherlands
[*] Author to whom any correspondence should be addressed.

E-mail: h.a.dijkstra@uu.nl

Keywords: numerical bifurcation analysis, primitive equation ocean model, multistability

Abstract

Both the Subpolar Gyre (SPG) and the Atlantic Meridional Overturning Circulation (AMOC) have been labeled as separate climate tipping systems, because characteristic transitions in flow patterns have been found in a hierarchy of models of each system. However, the precise connections between the two tipping systems are still unclear, in particular how they can affect their individual tipping behavior. Here, we present bifurcation diagrams of the combined SPG-AMOC system in a spatially three-dimensional North Atlantic Ocean model. We show that SPG tipping is associated with what we call 'Welander-snaking' behavior and the AMOC tipping with a Stommel back-to-back saddle-node bifurcation. The details of the bifurcation diagrams are shown to be sensitive to the formulation of the convective parameterization and the horizontal diffusivity of the model.

1. Introduction

The Atlantic Ocean Circulation is dominated by several large-scale currents, one prominent example being the Gulf Stream. The zonally integrated meridional volume transport of these currents is the Atlantic Meridional Overturning Circulation (AMOC). The AMOC is responsible for the northward heat transport which affects climate around the Atlantic basin Rahmstorf (2024). In the northern regions of the Atlantic, warm surface water from the upper branch of the AMOC is cooled and transformed into water of the deep AMOC branch. One of these regions where this water mass transformation occurs is the Subpolar Gyre (SPG) region, roughly between 50° N and 65° N, with currents in the Labrador and Irminger Seas as key components.

The stability of the connected SPG - AMOC system is an intriguing problem. In the Global Tipping Point Report Lenton *et al* (2025), , the SPG and AMOC are considered as two different tipping systems. The mechanism of destabilization of the AMOC is the salinity-advection feedback, where surface freshwater perturbations in the northern North Atlantic lead to a weakening of the AMOC. This leads to a decrease in northward salinity transport, amplifying the original freshwater perturbation Stommel (1961). The dominant mechanism of SPG tipping is the transition from a convective state to a non-convective state and vice-versa. Because the (stable) stratification in the SPG region is horizontally inhomogeneous, an unstable stratification can occur locally due to a negative surface freshwater perturbation (e.g. enhanced evaporation). This will induce vertical mixing which transports salinity upwards and hence will amplify the original perturbation Welander (1982).

The tipping of the AMOC under quasi-equilibrium surface freshwater forcing variations has now been found in a hierarchy of climate models, up to the CMIP5 version of the Community Earth System Model (CESM) van Westen *et al* (2024), and the strongly eddying version of the POP ocean-only model Van Westen, Kliphuis and Dijkstra (2025). Indications for weak AMOC states have been found in models participating in the Climate Model Intercomparison Project, phase 6 Jackson *et al* (2023), Baker *et al* (2025), also indicated as CMIP6 models, under large freshwater perturbation simulations. Further analyzes of the CESM quasi-equilibrium simulations has revealed that the salinity-advection feedback is

dominant in causing AMOC tipping Vanderborght *et al* (2025) and that it is very likely that a saddle-node bifurcation is involved van Westen, Vanderborght and Dijkstra (2025).

In analyzes of CMIP5 and CMIP6 model results, decadal cooling events were found in the SPG without a corresponding AMOC decline Sgubin *et al* (2017), Swingedouw *et al* (2021), Gu *et al* (2024). It has been suggested that these cooling events are caused by a positive feedback involving vertical mixing and freshwater anomalies. Reduced vertical mixing tends to cool and freshen the upper ocean, lowering its density if the effect of salinity on density is larger than that of temperature, further weakening vertical mixing. Such a convective feedback has similar properties as that causing the transition between convective and non-convective equilibrium states in the Welander (1982) model. However, in CMIP5/CMIP6 models it has not been demonstrated that the decadal cooling events, as mentioned above, are associated with transitions between different equilibria.

Because of the clear physical connection between the SPG and AMOC systems, it is interesting to investigate how tipping in one of these systems will affect the stability of the other. The stratification in the SPG will affect the density in the outcropping region of isopycnals in the 40°–60°N latitude band, which will influence the AMOC strength Bonan *et al* (2022), Vanderborght *et al* (2025). Hence, transitions in the SPG associated with changing patterns of convection are expected to influence the stability of the AMOC. On the other hand, an AMOC weakening will precondition the background stratification in the SPG region, affecting the locations where convection can take place and hence influence SPG stability Born and Stocker (2013).

Quasi-equilibrium freshwater forcing simulations with ocean-only models have provided indications of both SPG and AMOC tipping. In Rahmstorf (1994), small amplitude transitions in AMOC strength are found just before the AMOC undergoes a full transition to a collapsed state. These small transitions were due to the appearance of different convection patterns Rahmstorf (1996). In the VEROS model Lohmann *et al* (2024), a multitude of equilibrium states were found, in particular in the weak AMOC regime. Although not all, many of these equilibria seem related to different convection patterns in the SPG.

The main motivation for this paper is to explain the results in Lohmann *et al* (2024) on the multitude of equilibrium solutions in the SPG-AMOC system. We will approach this problem using techniques from numerical bifurcation theory, applied to a North Atlantic sector basin model of the SPG-AMOC system. This model is fit for purpose to study the multistability of this system, but otherwise lacks many processes to capture the specific AMOC-SPG interaction processes. The model will be described briefly in section 2, together with the numerical bifurcation techniques used. In section 3, we show the bifurcation diagram for our chosen reference case and study the sensitivity of the steady solutions to the details of the convection parameterization and the horizontal diffusivity in the model. A summary and discussion follows in section 4.

2. Model and methods

2.1. Model

We solve the steady primitive equations on a domain [262° E, 350° E] × [10° N, 74° N] and a maximum depth of 4 km. The grid has a horizontal resolution of 0.5° , and 16 depth layers with variable depth of about 20 m near the surface to 500 m near the bottom. Continental geometry and bottom topography are obtained by smoothing the ETOPO10 data. The horizontal resolution is relatively high to capture sufficient details of the continental geometry. The equations of the model can be found in De Niet *et al* (2007), but are for convenience shown here in the appendix.

A linear equation of state is used (for this study an adequate approximation as results will change only quantitatively when using a nonlinear equation state) with a thermal and saline volumetric expansion coefficients given by $\alpha_T = 10^{-4}\ K^{-1}$ and $\alpha_S = 4.2 \times 10^{-4}$, respectively. Constant eddy viscosities ($A_H = 2.5 \times 10^5\ m^2 s^{-1}$, $A_V = 1.0 \times 10^{-3}\ m^2 s^{-1}$) and eddy diffusivities ($K_H = 1.0 \times 10^3\ m^2 s^{-1}$, $K_V^0 = 1.0 \times 10^{-4}\ m^2 s^{-1}$). To keep the mixing schemes simple in this single-hemispheric configuration, no Gent–McWilliams Gent and McWilliams (1990), parameterization is used. The model is forced at the ocean-atmosphere surface by steady wind-stress and buoyancy flux fields, which are specified in section 3 below. There is no seasonality in the forcing, which makes the model less suited to study the transient interaction processes between the AMOC and SPG

Convection is parameterized as in De Niet *et al* (2007) where the vertical diffusivity is represented as

$$K_V = K_V^0 + \mathcal{F}\left(N^2\right) K_V^c, \tag{1}$$

where $N^2 = -g/\rho_0(\partial\rho/\partial z)$ is the buoyancy frequency, $K_V^c = \kappa K_V^0$ and g is the gravitational acceleration, $\rho_0 = 1000\ kg\ m^{-3}$ a reference density and ρ the actual density. The function $\mathcal{F}$ is chosen as

Den Toom *et al* (2011),

$$\mathcal{F}(x) = \max\left\{\tanh\left(-(\lambda x)^3\right), 0\right\}, \tag{2}$$

where $\lambda > 0$ controls the steepness of the transition. When $N^2 > 0$, the ocean is stably stratified ($\mathrm{d}\rho/\mathrm{d}z < 0$), the right hand side of (2) is zero and only background vertical mixing is applied. When $N^2 < 0$, additional vertical mixing occurs and it depends on λ for which value of N^2 full mixing with strength $K_V^0 + K_V^c = (1+\kappa)K_V^0$ is reached. Our reference values for the parameters in the convective parameterization are $\kappa = 10^3$ and $\lambda = 2 \times 10^3$. All standard values of the parameters in the model are also listed in the appendix.

As described in Den Toom *et al* (2011), the choice of the convective adjustment function (2) should prevent the occurrence of spurious equilibria. Furthermore, instead of mixing temperature and salinity, the mixing of density (difference between temperature and salinity) and spiciness (sum of temperature and salinity) is employed, the so-called 'density-mixing' variant in Den Toom *et al* (2011), also limiting the occurrence of spurious equilibria. We therefore expect that all bifurcation diagrams computed with our model will not show any spurious equilibria due to the choice of the convective parameterization.

2.2. Methods

The governing equations De Niet *et al* (2007), Thies *et al* (2009), are discretized on a so-called Lorentz grid, consisting of an equidistant grid for $x_i, i = 1, \ldots N$ and $y_j, j = 1, \ldots, M$, and a non-equidistant grid $z_k, j = 1, \ldots, L$ using central differences. This results in $d = 6 \times N \times M$ ordinary differential Equations, where d is the total number of degrees of freedom. Because of the time-independent forcing, they can be written as an autonomous dynamical system of the form

$$\frac{\partial \mathbf{u}}{\partial t} = \mathbf{F}(\mathbf{u}, \mu). \tag{3}$$

Here $\mathbf{u}$ is the state vector and μ is a control parameter. With $N = 176, M = 128$ and $L = 16$, the dimension of the resulting dynamical system $d = 2\,162\,688$.

To determine branches of steady solutions of the equations (3) as one of the parameters, say μ, is varied, the pseudo-arclength method Keller (1977), is used. The branches $(\mathbf{u}(s), \mu(s))$ are parameterized by an 'arclength' parameter s. An additional equation is obtained by 'normalizing' the tangent along the branch, i.e.

$$\dot{\mathbf{u}}_0^T(\mathbf{u} - \mathbf{u}_0) + \dot{\mu}_0(\mu - \mu_0) - \Delta s = 0, \tag{4}$$

where $(\mathbf{u}_0, \mu_0)$ is an analytically known starting solution or a previously computed point on a particular branch and Δs is the step length. The dot indicates differentiation with respect to the arclength parameter s.

Euler-Newton continuation is used to solve the system of equations (3) and (4). The $(d+1) \times (d+1)$ Jacobian matrix $J(s)$ of (3) and (4) along a branch is given by

$$\mathcal{J}(s) = \begin{bmatrix} A & \mathbf{F}_\mu \\ \dot{\mathbf{u}_0}^T & \dot{\mu}_0, \end{bmatrix} \tag{5}$$

where A is the matrix of derivatives of $\mathbf{F}$ with respect to $\mathbf{u}$ and $\mathbf{F}_\mu$ the derivative with respect to the parameter μ. The Jacobian $J(s)$ is determined analytically from the discrete equations.

For each of the steady states, we also consider the evolution of infinitesimally small disturbances on a particular steady state. Linearizing the equations (3) in the amplitude of the perturbations and separating the equations for these disturbances in time, an elliptic eigenvalue problem is obtained for the complex growth rate $\sigma = \sigma_r + \mathrm{i}\sigma_i$ of each perturbation. When this elliptic eigenvalue problem is discretized, an algebraic eigenvalue problem is obtained as

$$A\mathbf{x} = \sigma\mathbf{x}. \tag{6}$$

A steady state is linearly stable if $\sigma_r < 0$ for all eigenvalues; if at least one of the eigenvalues σ has a positive real part, then the steady state is unstable.

The software used here is the ocean component of the 'Implicit Earth system Model of Intermediate Complexity', in the version publicly available through https://github.com/jthies/i-emic/releases/tag/SPG-AMOC_paper. The parallel implementation is described in Thies *et al* (2009), and the direct sparse solver method MUMPS is used for the determine solutions to the linear systems for the Jacobian $J(s)$ Wubs and Dijkstra (2023). Note that we do not compute any time-dependent trajectories, such as in quasi-equilibrium simulations; we solely determine the steady state directly versus parameters.

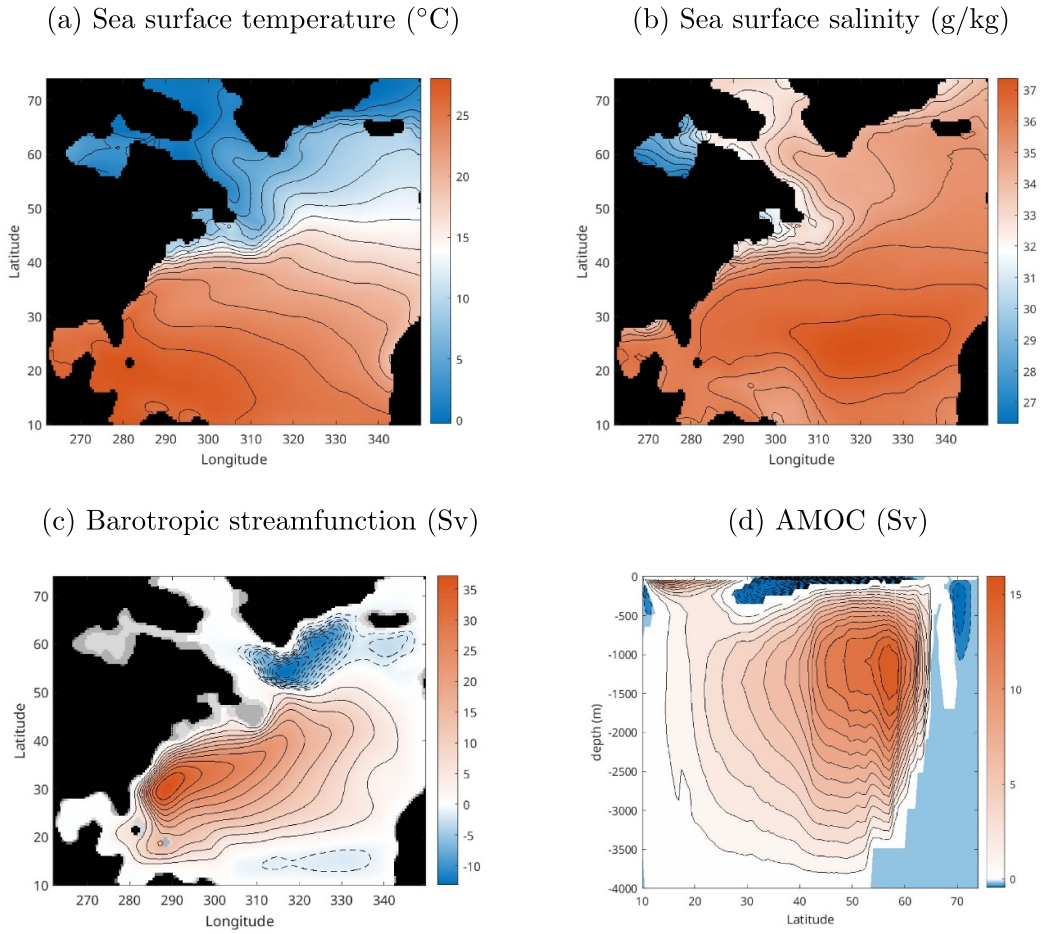

Figure 1. Properties of the reference solution: (a) sea surface temperature, (b) sea surface salinity, (c) barotropic stream function and (d) meridional overturning stream function (AMOC).

3. Results

We first compute a reference solution under restoring forcing for temperature and salinity (section 3.1). From this solution, we diagnose the surface freshwater flux and then add an additional localized freshwater flux in the northern North Atlantic. The bifurcation diagram in the parameter measuring the strength of this additional freshwater flux, with the analysis of the properties of the associated steady states are the main results in section 3.2 In section 3.3, we determine the sensitivity of the bifurcation diagram with respect to horizontal diffusivity K_{H} and the steepness parameter λ in the convection parameterization.

3.1. Reference solution

The restoring salinity and temperature forcing are chosen as the long-term mean surface fields from the Levitus (1994) dataset, with a restoring time scale of 75 d. Often, a larger restoring time scale is chosen for salinity, which will affect the diagnosed freshwater flux (discussed below). However, this will not qualitatively change the overall bifurcation diagram. The mean wind-stress forcing field from Trenberth *et al* (1989) is used. The reference solution is obtained by continuation in a so-called 'homotopy' parameter h_α which simultaneously increases the surface buoyancy forcing and wind-stress forcing from zero ($h_\alpha = 0$) to a realistic strength ($h_\alpha = 1$). The sea surface temperature and sea surface salinity, basically reflecting that of the (restoring) forcing are shown in figures 1(a) and (b). The meridional temperature and salinity differences over this region are about 25 °C and about 5 g kg^{-1}, respectively. The barotropic streamfunction and meridional overturning streamfunction are plotted in figures 1(c) and (d), respectively. The subtropical (subpolar) gyre has a strength of about 25 Sv (10 Sv) and the AMOC strength (the maximum value of the meridional overturning stream function) is about 16 Sv (at about 55° N and 1250 m depth). These values (in particular of the barotropic stream function) are smaller than in observations but reasonable for these type of idealized models. Because the North Atlantic domain only extends down to 10° N, the AMOC pattern consists of one cell. Indeed, the bottom water

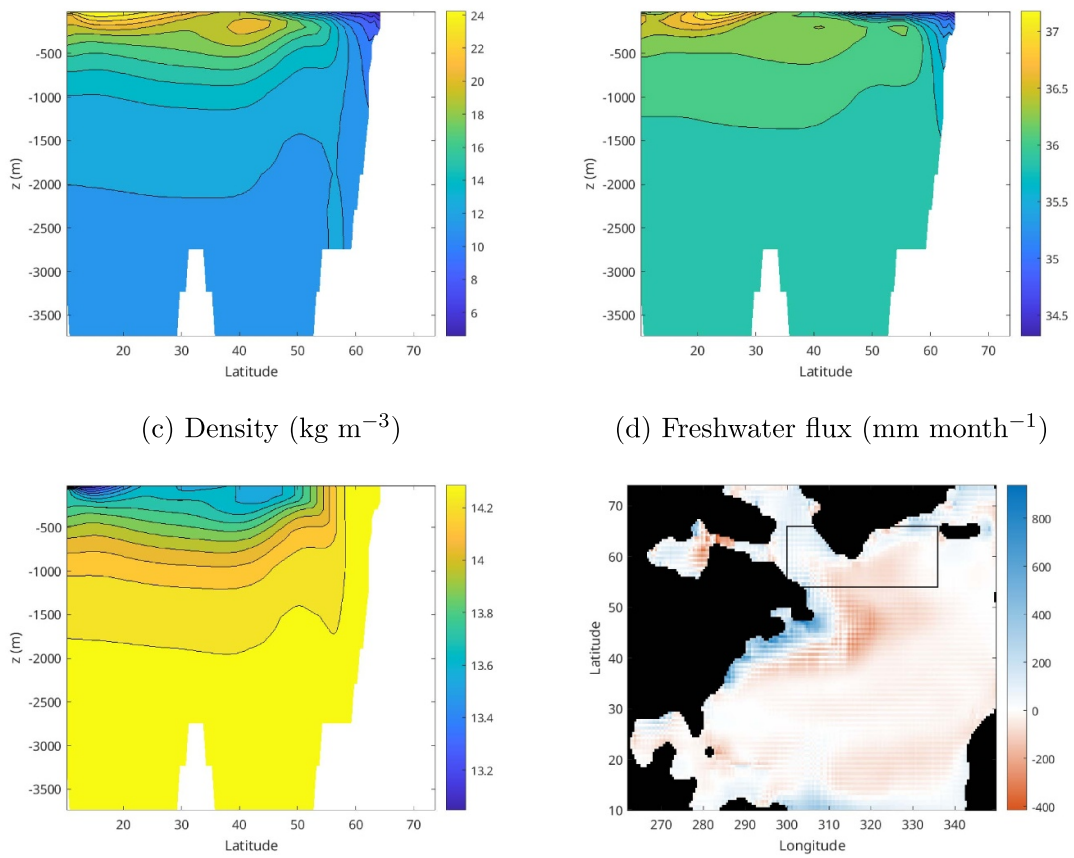

Figure 2. Properties of the reference solution: Latitudinal section of (a) temperature, (b) salinity, and (c) density ($\rho - \rho_0$, where $\rho_0 = 1000$ kg m^{-3}) along a longitude 320° E. (d) Surface freshwater flux ($\bar{F}_S$ in (7) diagnosed from the reference solution. The rectangle indicates the domain over which the perturbation freshwater flux $F^p{}_S$ in (7) is applied.

component (the Antarctic Bottom Water) cannot be adequately represented in such a limited geometry. The effect of the AMOC due to the wind-driven Ekman cells can be distinguished at the top of the domain.

To demonstrate the effect of the convective parameterization, a section at 320°E of temperature, salinity and density is plotted in figures 2(a)–(c), respectively. All fields are quite homogeneous below 1500 m depth and vertically well mixed in the northern part of the domain. Figure 2(c) shows that the convective adjustment scheme generates a stably stratified reference solution in the model. The surface freshwater flux diagnosed from the reference solution (figure 2(d)), indicated by $\bar{F}_S$ below, shows that freshwater (blue areas, positive values) or salinity (red areas, negative values) is needed to maintain the steady Levitus (1994) surface salinity field. For example, a positive freshwater flux has to be prescribed to maintain the low surface salinity values near New Foundland.

3.2. Bifurcation diagram

Starting from the reference solution, we next prescribe the freshwater flux F_S as

$$F_S(\phi,\theta) = \bar{F}_S + \gamma_p F^p{}_S + Q, \tag{7}$$

where $\bar{F}_S$ was shown in figure 2(d). The perturbation freshwater flux $F^p{}_S$ is unity over the domain [300° E,336° E] × [54° N,66° N] (see box in figure 2(d) and zero elsewhere. We use γ_p as the control parameter in the bifurcation analysis and Q is determined such that

$$\int_{\mathcal{S}_{oa}} F_S(\phi,\theta)\cos\theta \; \mathrm{d}\phi\,\mathrm{d}\theta = 0, \tag{8}$$

where $\mathcal{S}_{oa}$ is the ocean-atmosphere surface, such that salinity is conserved when varying γ_p.

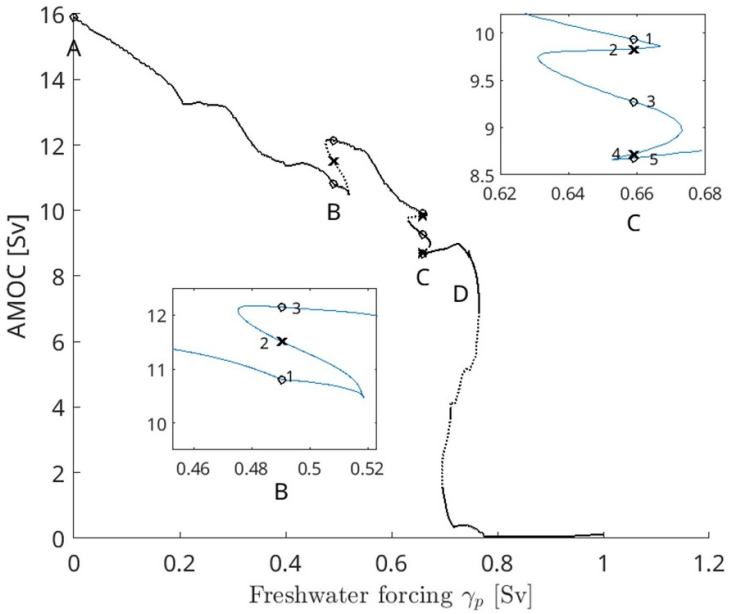

Figure 3. Bifurcation diagram, showing the maximum of the AMOC strength below 500 m depth and north of 30° N versus the control parameter γ_p in (7). Branches with linearly stable steady states are drawn while branches with unstable steady states are dashed. Insets are magnifications of the W-snaking regions and the solution labels refer to steady states analyzed in section 3.3.

The resulting bifurcation diagram is shown in figure 3, with the reference solution, indicated by a label A, located at $\gamma_p = 0$. For small γ_p, the AMOC strength decreases monotonically, but for larger values several saddle-node bifurcations occur (near locations B and C). After passing through the region near C, the AMOC reaches a final saddle-node bifurcation, indicated by D, where the strength rapidly decreases with γ_p. In general, increasing (decreasing) parameter branches in γ_p indicate linearly stable (unstable) steady states.

What is interesting in this bifurcation diagram is the occurrence of a multitude of saddle-node bifurcations. We will refer to this behavior as Welander snaking (in short W-snaking) describing the many turns in the bifurcation diagram. Whereas the snaking terminology has so far been used to describe the intertwining of periodic orbits, often referred to as homoclinic snaking Beck *et al* (2009), W-snaking here describes the intertwining of steady states. Note that the part of the stable solutions of the bifurcation diagram qualitatively looks similar to the solution structure of the VEROS model Lohmann *et al* (2024), with also indications for W-snaking behavior in a parameter interval close to where the AMOC collapses.

3.3. Analysis

The patterns of the meridional overturning stream function at the reference solution (A) and at $\gamma_p = 0.49$ Sv (B_1) and $\gamma_p = 0.66$ Sv (C_1) are plotted in figures 4(a), (b) and (d), respectively. The pattern in figure 4(a) is the same as in figure 1(d), but is shown here again for easier comparison with the other solutions. Due to the input of fresh water, the sinking in the north is reduced in state B_1 with respect to state A and most of the deep sinking occurs at 50° N.

The AMOC differences between stable states B_3 and B_1 occur (figure 4(c)) mostly near the upwelling region at 25°N and the downwelling region at 50°N. Because the upwelling strengthens, also the AMOC strength increases in B_3 compared to B_1. The maximum AMOC shifts southward and occurs at shallower depth. State B_2 is a so-called edge state that is not further considered here, but is interesting for studying transitions between B_1 and B_3 Lohmann and Lucarini (2024). The AMOC at state C_1 (figure 4(d)) is further reduced in amplitude compared to state B_1, but the pattern has not changed much, except in the 20°N–30°N region where the surface circulation strengthens. The AMOC difference patterns between C_3 and C_1 (figure 4(e)) and between C_5 and C_1 (figure 4(f)) show tiny differences concentrated near the downwelling region slightly south of 50°N. In summary, in the W-snaking γ_p interval, the AMOC patterns only slightly change between the different stable solutions for the same γ_p.

To determine what causes these slight changes in AMOC strength and pattern, we compute the mixed-layer depth. This is defined as the depth for which the density is a factor 1.005 larger than the surface density. Note that our model does not include an explicit mixed-layer model, so the mixed-layer

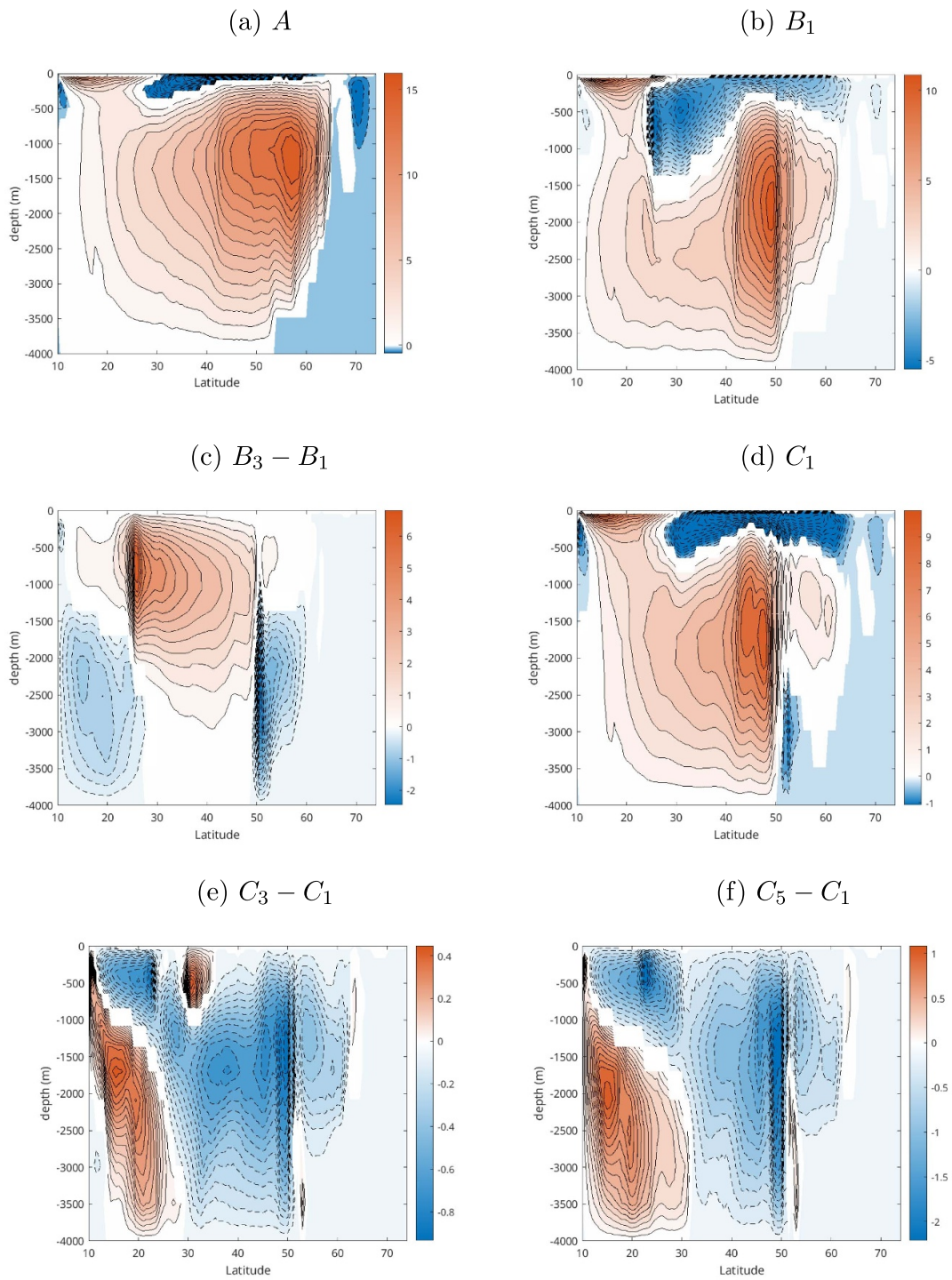

Figure 4. Pattern of the AMOC of (a) the reference state A, (b) the state B_1 and (d) the state C_1. (c) Difference pattern between the AMOC of state B_3 and state B_1. (e) Difference pattern between the AMOC at state C_3 and state C_1. (f) Difference pattern between the AMOC at state C_5 and state C_1. Labels refer to those shown in figure 3.

depth is just determined by the vertical mixing coefficient in the convective-adjustment scheme. The patterns of the mixed layer depth at the reference solution (A) and at $\gamma_p = 0.49$ Sv (B_1) and $\gamma_p = 0.66$ Sv (C_1) are shown in figures 5(a), (b) and (d), respectively. The deepest mixed layers occur in the SPG region in all three states with shallower depths south of 50°S. The main difference between states A and B_1 are in the Irminger Sea region where in B_1 the mixed layer significantly shallows compared to that in A. In state C_1, the region of deepest mixed layer has slightly shifted southward compared to that in B_1. The mixed-layer depth differences between states B_3 and B_1 occur (figure 5(c)) in very localized areas near 50°N and over a broader low-latitude area near Africa. The same holds for the differences in mixed-layer depth between C_1 (figure 5(e)) and C_3 and between C_5 and C_1 (figure 5(f)).

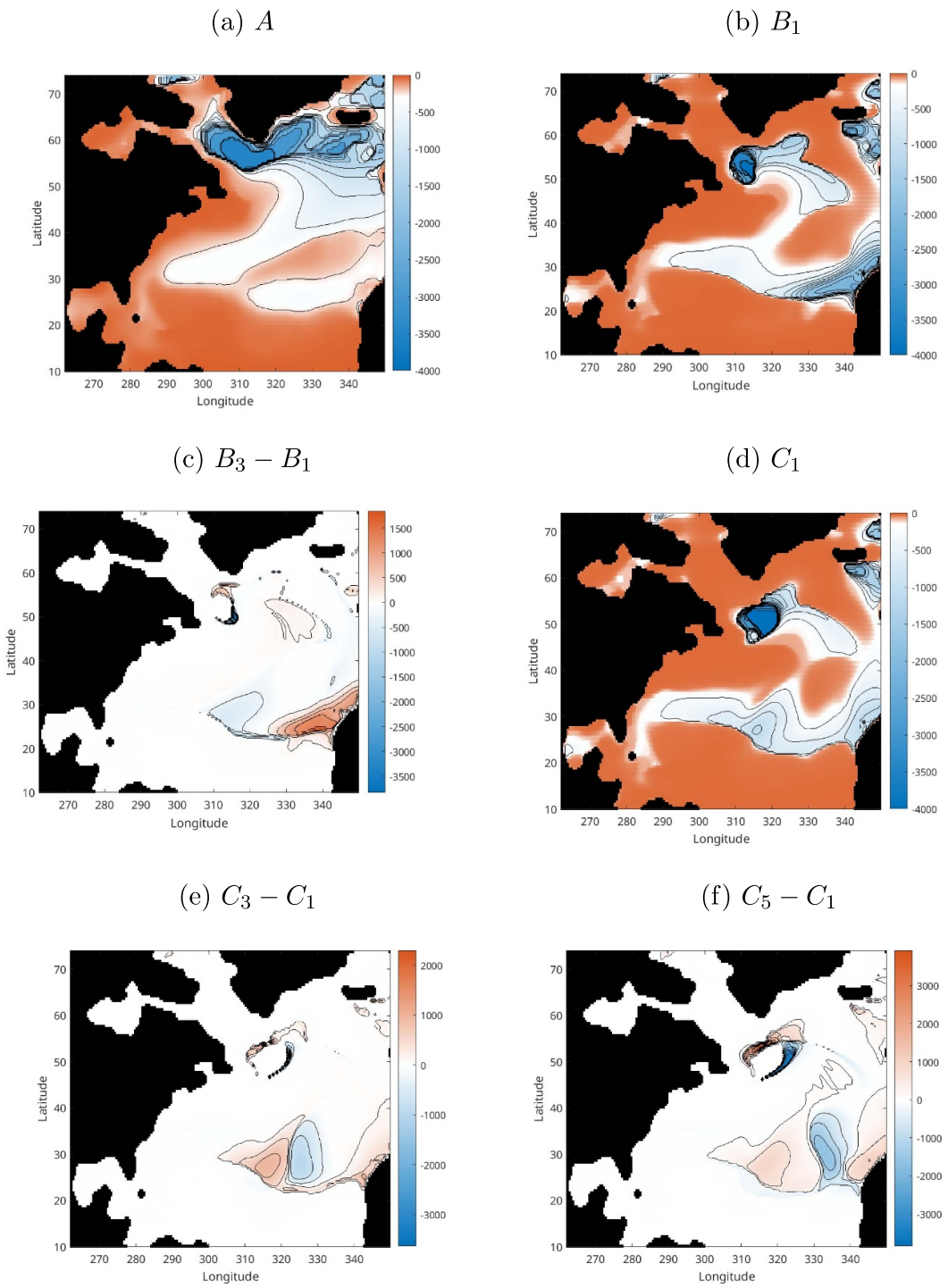

Figure 5. Mixed layer depth $d(x,y)$ here defined as the value of $z = d(x,y)$ where $\rho(\phi,\theta,d(\phi,\theta)) = 1.005 \times \rho(\phi,\theta,0)\,\mathrm{kg\,m^{-3}}$, for (a) reference state A, (b) the state B_1 and (d) the state C_1. (c) Difference pattern between the mixed-layer depth of state B_3 and state B_1. (e) Difference pattern between the mixed-layer depth at state C_3 and state C_1. (f) Difference pattern between the mixed-layer depth at state C_5 and state C_1. Labels refer to those shown in figure 3.

The results in figures 4 and 5 show that W-snaking behavior is associated with very localized changes in convection, visible as mixed-layer depth differences. These do not occur directly in the SPG region in this model, but slightly south of it, which is due to the background stratification and the choice of the surface forcing. The surface forcing controls the region where the switch function in (2) is sensitive to changes in γ_p. The AMOC strength is affected by different locations where convection occurs, due to slight changes in horizontal density differences, and hence slightly different AMOC patterns occur.

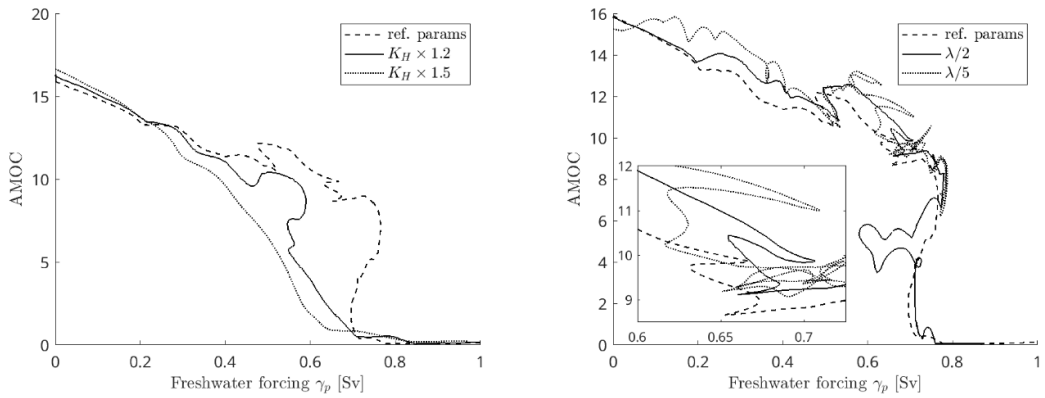

Figure 6. Bifurcation diagrams (similar to figure 3) for different values of (a) K_H and (b) of λ to determine the sensitivity of the W-snaking behavior to horizontal diffusion and steepness of the convective parameterization. The bifurcation diagram of the reference case (figure 3) is plotted as the dashed curve for comparison. The stability of the steady solutions along the branches is not indicated. In panel (b), a magnification of the W-snaking region is shown, illustrating the complexity of the bifurcation diagram.

3.4. Sensitivity analysis

Previous work (Den Toom *et al* 2011, Bailie and Krauskopf 2024) has indicated that the occurrence of the W-snaking behavior is dependent on the horizontal diffusion coefficient and on the formulation of the convection parameterization. To investigate this sensitivity, we vary both independently (through parameters K_H and λ) and the resulting bifurcation diagrams are shown in figures 6(a) and (b).

With only 1.5 times the standard horizontal diffusion, the W-snaking behavior disappears (figure 6(a)). Actually, all saddle-node bifurcations disappear, also the one responsible for the AMOC collapse. The AMOC now gradually declines to zero when γ_p is increased. With a factor 1.2 increase in K_H, some saddle-node bifurcation are still present, but the multi-stable regime is much smaller than that of the reference case. A larger value of K_H smears out the local density differences that occur through the switch from convective to non-convective states and hence erases the differences between the states.

On the contrary, when the steepness parameter λ in the convective parameterization (2) is decreased, the W-snaking behavior intensifies and several more saddle-node bifurcations appear (figure 6(b)). Note that intersections of the branches do not indicate transcritical bifurcations, but are just due to the chosen norm to display the state vector. For a smaller value of λ, a larger range of density differences occurs where larger vertical mixing (due to the factor K_V^c) occurs. As this can happen at more locations, a more intense W-snaking behavior is found, but for each value of λ, W-snaking is still limited to the parameter interval where the AMOC is relatively weak. The results demonstrate the large sensitivity of the W-snaking behavior to the steepness parameter in the convective parameterization. This can also be interpreted in terms of the quasi-potential landscape Lucarini and Bódai (2020), where a higher diffusivity leads to a smoother landscape and local features are lost.

4. Summary and discussion

In this paper, we computed bifurcation diagrams of a relatively high-resolution (0.5° horizontal resolution) three-dimensional primitive equation ocean model on a limited North Atlantic sector. The reference state of the model is calculated under (observed) restoring conditions for temperature and salinity and a prescribed steady wind-stress field. Technically, applying numerical continuation methods to such a high-dimensional dynamical system (with more than 2 million degrees of freedom), is quite an accomplishment Thies *et al* (2009), Dijkstra *et al* (2015), Wubs and Dijkstra (2023), in particular because the Jacobian matrix of the model is highly ill-conditioned.

When the strength of a localized northern North Atlantic perturbation freshwater flux is taken as control parameter, multiple saddle-node bifurcations occur. This results in parameter intervals where

multiple stable states having slightly different AMOC strengths exist. The solutions intertwine over a relatively small parameter interval and the transitions are between states which have slightly different locations where convection occurs (as here shown through the analysis of the mixed-layer depth). Based on Welander (1982), we suggested to call this bifurcation behavior 'Welander snaking' (in short W-snaking).

Detailed analysis of the Welander (1982) model by Bailie and Krauskopf (2024) shows the complexity of the dynamics of the transitions between convective and non-convective states. The representation of the threshold behavior in density (ε in Bailie and Krauskopf 2024) strongly affects these transitions. In our model, we find that when the horizontal diffusion is increased, the W-snaking disappears because then the buoyancy anomalies associated with convection are smeared out and hence convection becomes less local. On the other hand, W-snaking is dependent on the details of the convection parameterization, in particular the steepness parameter, as this will determine where exactly convective transitions occur, in agreement with the results in Bailie and Krauskopf (2024).

The W-snaking mechanism can explain the results on multi-stability involving different convection patterns as in Rahmstorf (1995) and Lohmann *et al* (2024). Indeed, in their quasi-equilibrium freshwater forcing simulations, multiple stable (near-)equilibria (with slightly different AMOC values) are found which are related to different patterns of convection, i.e. of the mixed layer depth. The bifurcation diagram here provides information on the effect of AMOC strength on the occurrence of W-snaking, which occurs only when the AMOC is relatively weak. The reason is that the northern North Atlantic becomes more buoyant under a weaker AMOC allowing the convective states to be inhibited by surface forcing more easily. Also in Rahmstorf (1995) and Lohmann *et al* (2024) the parameter regimes where multiple steady states occur with slightly different AMOC strengths, are in the weak AMOC regime.

Our results can also help to interpret CMIP5/CMIP6 model simulation results on SPG cooling events such as those in Swingedouw *et al* (2021) and Gu *et al* (2024). In these models, the forcing over the SPG is stochastic (e.g. the variability due to atmospheric forcing) which also affects the way the stratification threshold for convection is exceeded. Based on our deterministic model results, such stochastic variations would induce transitions from convective to non-convective states in the W-snaking regime, with subsequent effects on sea surface temperature. The actual situation is, of course, much more complicated because there may also be mixed layer deepening under a stable stratification and there may be compensating mixed-layer variations during convection, for example caused by the winds or due to sea-ice variations.

There is an important loose end to this study which needs to be addressed in future work, i.e. the issue whether W-snaking behavior can also lead to spurious equilibria. When convection occurs at a specific location, neighboring cells may also undergo a convective transition (or not) because there are lateral fluxes connecting these cells, which depend on advective-diffusive processes. Analysis of the one-dimensional (vertical) continuum model of convection, where the lateral flux is represented as a relaxation to a background temperature and salinity profile has shown that spurious equilibria can occur Vellinga (1998), Den Toom *et al* (2011). Here, we have followed their recommendations for the convective parameterization to avoid such spurious equilibria, but that does not guarantee their absence as the flow configuration here is three-dimensional.

In addition, in global ocean and climate models much more complicated convection schemes are used, such as the KPP Large *et al* (1994) scheme (used in the CESM) and the Gaspar *et al* (1990) scheme (used in the VEROS model), and it is far from trivial to extract relevant properties of the convective parameterization (e.g. steepness parameter and density threshold) from these schemes. The connection between these schemes and those of the convective parameterizations in the idealized models should be clarified to obtain information whether the cooling events found in these models are caused by convective transitions and whether these are spurious are not.

In the most recent global tipping point report Lenton *et al* (2025), the SPG and the AMOC are considered as two separate tipping systems. Based on the results of this study, one can identify the AMOC tipping with the saddle-node bifurcation associated with the Stommel salinity advection feedback and the SPG tipping with the saddle-nodes due to W-snaking. Indeed, the changes in AMOC strength are relatively small when a transition occurs between near steady states due to W-snaking. Hence, from a bifurcation analysis point of view, such a separation in tipping systems is justified.

Acknowledgments

The work of H A D is funded by the European Research Council through the ERC-AdG Project TAOC (PI: Dijkstra, Project 101055096). The authors acknowledge the use of computational resources of the

DelftBlue supercomputer, provided by Delft High Performance Computing Centre (www.tudelft.nl/dhpc).

Data availability statement

All data that support the findings of this study are included within the article (and any supplementary files).

Author contributions

Jonas Thies 0000-0001-9231-9999
Data curation (lead), Formal analysis (lead), Investigation (supporting), Methodology (lead), Resources (equal), Software (equal), Validation (equal), Visualization (equal), Writing – review & editing (equal)

Henk A Dijkstra 0000-0001-5817-7675
Conceptualization (equal), Funding acquisition (equal), Investigation (equal), Methodology (equal), Project administration (equal), Resources (equal), Supervision (equal), Validation (equal), Visualization (equal), Writing – original draft (equal)

Appendix. Model equations

We consider flows in a spherical sector bounded by longitudes ϕ_w and ϕ_e and by latitudes θ_s and θ_n. The ocean basin has a bottom topography $z=-D(\phi,\theta)$ with mean $z=-D_0$ and a nondeformable ocean-atmosphere boundary $z=0$. The flows in this domain are forced by a heat flux $Q_{\rm H}$ (in Wm^{-2}), a zonal wind stress field (τ^ϕ,τ^θ) (in Pa) and a virtual salt flux $Q_{\rm S}$ (in ms^{-1}).

In the restoring case, the heat flux $Q_{\rm H}$ is proportional to the temperature difference between the sea-surface temperature T and a prescribed temperature $T_{\rm S}$, i.e.

$$Q_{\rm H}=-\lambda_{\rm T}\left(T-T_{\rm S}\right) \tag{9}$$

where $\lambda_{\rm T}$ (in $\mathrm{Wm}^{-2}\mathrm{K}^{-1}$) is a constant exchange coefficient. The virtual salt flux $Q_{\rm S}$ is similarly given by

$$Q_{\rm S}=-\lambda_{\rm S}\left(S-S_{\rm S}\right) \tag{10}$$

where $\lambda_{\rm S}$ (in ms^{-1}) is an exchange coefficient. Both wind and buoyancy forcing are distributed as a body forcing over the first (upper) layer of the ocean model having a depth H_m.

Temperature and salinity differences in the ocean cause density differences according to

$$\rho=\rho_0\left(1-\alpha_{\rm T}\left(T-T_0\right)+\alpha_{\rm S}\left(S-S_0\right)\right) \tag{11}$$

where $\alpha_{\rm T}$ and $\alpha_{\rm S}$ are the volumetric expansion coefficients and T_0, S_0 and ρ_0 are reference quantities. We use the Boussinesq and hydrostatic approximations. With r_0 and Ω being the radius and angular velocity of the Earth, the governing equations for the zonal, meridional and vertical velocity u,v and w and the dynamic pressure p (the hydrostatic part has been subtracted) become

$$\frac{Du}{\mathrm{d}t}-\frac{uv\tan\theta}{r_0}-2\Omega\ v\sin\theta+\frac{1}{\rho_0 r_0\cos\theta}\frac{\partial p}{\partial\phi}$$

$$=A_{\rm V}\frac{\partial^2 u}{\partial z^2}+A_{\rm H}L_u\left(u,v\right)+\frac{\tau_0}{\rho_0 H_m}\tau^\phi\mathcal{G}\left(z\right) \tag{12a}$$

$$\frac{Dv}{\mathrm{d}t}+\frac{u^2\tan\theta}{r_0}+2\Omega\ u\sin\theta+\frac{1}{\rho_0 r_0}\frac{\partial p}{\partial\theta}$$

$$=A_{\rm V}\frac{\partial^2 v}{\partial z^2}+A_{\rm H}L_v\left(u,v\right)+\frac{\tau_0}{\rho_0 H_m}\tau^\theta\mathcal{G}\left(z\right) \tag{12b}$$

$$\frac{\partial p}{\partial z}=\rho_0 g\left(\alpha_{\rm T}T-\alpha_{\rm S}S\right) \tag{12c}$$

Table 1. Standard values of parameters in the ocean model.

$2\Omega = 1.4 \cdot 10^{-4}[s^{-1}]$	$r_0 = 6.4 \cdot 10^{6}[m]$
$C_\mathrm{p} = 4.2 \cdot 10^{3}[\mathrm{J(kgK)}^{-1}]$	$\tau_\mathrm{T} = 7.5 \cdot 10^{1}[\mathrm{d}]$
$\tau_\mathrm{S} = 7.5 \cdot 10^{1}[\mathrm{d}]$	$\alpha_\mathrm{T} = 1.0 \cdot 10^{-4}[\mathrm{K}^{-1}]$
$\alpha_\mathrm{S} = 4.2 \cdot 10^{-4}[-]$	$\rho_0 = 1.0 \cdot 10^{3}[\mathrm{kg\ m}^{-3}]$
$H_m = 20$ [m]	$A_\mathrm{V} = 1.0 \cdot 10^{-3}[\mathrm{m^2 s^{-1}}]$
$A_\mathrm{H} = 2.5 \cdot 10^{5}[\mathrm{m^2 s^{-1}}]$	$K_\mathrm{H} = 1.0 \cdot 10^{3}[\mathrm{m^2 s^{-1}}]$
$K_\mathrm{V}^0 = 1.0 \cdot 10^{-4}[\mathrm{m^2 s^{-1}}]$	$K_\mathrm{V}^c = \kappa K_\mathrm{V}^0[\mathrm{m^2 s^{-1}}]$
$\kappa = 1.0 \cdot 10^{3}$ [–]	$\lambda = 2.0 \cdot 10^{3}$ [–]

$$\frac{\partial w}{\partial z} + \frac{1}{r_0 \cos\theta}\left(\frac{\partial u}{\partial \phi} + \frac{\partial (v\cos\theta)}{\partial \theta}\right) = 0 \tag{12d}$$

$$\frac{DT}{\mathrm{d}t} + \nabla_\mathrm{H}.(K_\mathrm{H}\nabla_\mathrm{H} T) + \frac{\partial}{\partial z}\left(K_\mathrm{V}\frac{\partial T}{\partial z}\right) = \frac{(T_\mathrm{S} - T)}{\tau_\mathrm{T}}\mathcal{G}(z) \tag{12e}$$

$$\frac{DS}{\mathrm{d}t} + \nabla_\mathrm{H}.(K_\mathrm{H}\nabla_\mathrm{H} S) + \frac{\partial}{\partial z}\left(K_\mathrm{V}\frac{\partial S}{\partial z}\right) = \frac{(S_\mathrm{S} - S)}{\tau_\mathrm{S}}\mathcal{G}(z) \tag{12f}$$

where $\mathcal{G}(z) = \mathcal{H}(z/H_m + 1)$ and $\mathcal{H}$ is a continuous approximation of the Heaviside function. Furthermore, C_p is the constant heat capacity and $\tau_\mathrm{T} = \rho_0 C_\mathrm{p} H_m/\lambda_\mathrm{T}$ and $\tau_\mathrm{S} = H_m/\lambda_\mathrm{S}$ are the surface adjustment time scales of heat and salt, respectively. In addition,

$$\begin{aligned}
\frac{D}{\mathrm{d}t} &= \frac{\partial}{\partial t} + \frac{u}{r_0\cos\theta}\frac{\partial}{\partial \phi} + \frac{v}{r_0}\frac{\partial}{\partial \theta} + w\frac{\partial}{\partial z} \\
L_u(u,v) &= \nabla_\mathrm{H}^2 u + \frac{u\cos 2\theta}{r_0^2\cos^2\theta} - \frac{2\sin\theta}{r_0^2\cos^2\theta}\frac{\partial v}{\partial \phi} \\
L_v(u,v) &= \nabla_\mathrm{H}^2 v + \frac{v\cos 2\theta}{r_0^2\cos^2\theta} + \frac{2\sin\theta}{r_0^2\cos^2\theta}\frac{\partial u}{\partial \phi} \\
\nabla_\mathrm{H}^2 &= \frac{1}{r_0^2\cos\theta}\left[\frac{\partial}{\partial \phi}\left(\frac{1}{\cos\theta}\frac{\partial}{\partial \phi}\right) + \frac{\partial}{\partial \theta}\left(\cos\theta\frac{\partial}{\partial \theta}\right)\right].
\end{aligned}$$

In the equations (12*a*) and (12*b*), A_H and A_V are the horizontal and vertical momentum (eddy) viscosity which we will take constant.

The vertical diffusivity is chosen as

$$K_\mathrm{V} = K_\mathrm{V}^0 + \mathcal{F}\left(N^2\right) K_\mathrm{V}^c, \tag{13}$$

with $N^2 = -g/\rho_0(\partial\rho/\partial z)$ and

$$\mathcal{F}(x) = \max\left\{\tanh\left(-(\lambda x)^3\right), 0\right\}. \tag{14}$$

Slip conditions are assumed at the bottom boundary, while at all lateral boundaries no-slip conditions are applied. At all lateral boundaries and the bottom boundary, the heat flux is zero. As the forcing is represented as a body force over the first layer, slip and no-flux conditions apply at the ocean surface. Hence, the boundary conditions are

$$z = -D, 0: \quad \frac{\partial u}{\partial z} = \frac{\partial v}{\partial z} = w = \frac{\partial T}{\partial z} = \frac{\partial S}{\partial z} = 0 \tag{15a}$$

$$\phi = \phi_w, \phi_e: \quad u = v = w = \frac{\partial T}{\partial \phi} = \frac{\partial S}{\partial \phi} = 0 \tag{15b}$$

$$\theta = \theta_s, \theta_n: \quad u = v = w = \frac{\partial T}{\partial \theta} = \frac{\partial S}{\partial \theta} = 0. \tag{15c}$$

Standard values of the parameters are listed in table 1.

References

Bailie J and Krauskopf B 2024 Bifurcation analysis of a conceptual model for vertical mixing in the North Atlantic *Physica D* **460** 134077

Baker J A, Bell M J, Jackson L C, Vallis G K, Watson A J and Wood R A 2025 Continued Atlantic overturning circulation even under climate extremes *Nature* **638** 987–94

Beck M, Knobloch J, Lloyd D J B, Sandstede B and Wagenknecht T 2009 Snakes, ladders and isolas of localized patterns *SIAM J. Math. Anal.* **41** 936–72

Bonan D B, Thompson A F, Newsom E R, Sun S and Rugenstein M 2022 Transient and equilibrium responses of the Atlantic overturning circulation to warming in coupled climate models: The role of temperature and salinity *J. Clim.* **35** 5173–93

Born A and Stocker T F 2013 Two stable equilibria of the Atlantic Subpolar Gyre *J. Phys. Oceanogr.* **44** 131003141459004

De Niet A, Wubs F, van Scheltinga A T and Dijkstra H A 2007 A tailored solver for bifurcation analysis of ocean-climate models *J. Comput. Phys.* **227** 654–79

Den Toom M, Dijkstra H A and Wubs F W 2011 Spurious multiple equilibria introduced by convective adjustment *Ocean Modelling* **38** 126–37

Dijkstra H A *et al* 2015 Numerical bifurcation methods and their application to fluid dynamics: analysis beyond simulation *Commun. Comput. Phys.* **15** 1–45

Gaspar P, Grégoris Y and Lefevre J-M 1990 A simple eddy kinetic energy model for simulations of the oceanic vertical mixing: Tests at station papa and long-term upper ocean study site *J. Geophys. Res.: Oceans* **95** 16179–93

Gent P and McWilliams J C 1990 Isopycnal mixing in ocean circulation models *J. Phys. Oceanogr.* **20** 150–5

Gu Q, Gervais M, Danabasoglu G, Kim W M, Castruccio F, Maroon E and Xie S-P 2024 Wide range of possible trajectories of North Atlantic climate in a warming world *Nat. Commun.* **15** 4221

Jackson L C *et al* 2023 Understanding AMOC stability: the North Atlantic Hosing Model Intercomparison Project *Geosci. Model Dev.* **16** 1975–95

Keller H B 1977 Numerical solution of bifurcation and nonlinear eigenvalue problems *Applications of Bifurcation Theory* ed P H Rabinowitz (Academic) (available at: http://pascal-francis.inist.fr/vibad/index.php?action=getRecordDetail&idt=PASCAL7830413329)

Large W G, McWilliams J C and Doney S C 1994 Oceanic vertical mixing: A review and a model with a nonlocal boundary layer parameterization *Rev. Geophys.* **32** 363–403

Lenton T M *et al* 2025 *The Global Tipping Points Report 2025* (University of Exeter) (https://doi.org/10.5281/zenodo.18163977)

Levitus S 1994 World Ocean Atlas 1994 *Temperature* vol 4 (NOAA/NESDIS E, US Department of Commerce) pp 1–117 (available at: https://repository.library.noaa.gov/view/noaa/1381)

Lohmann J, Dijkstra H A, Jochum M, Lucarini V and Ditlevsen P D 2024 Multistability and intermediate tipping of the Atlantic Ocean circulation *Sci. Adv.* **10** eadi4253

Lohmann J and Lucarini V 2024 Melancholia states of the atlantic meridional overturning circulation *Phys. Rev. Fluids* **9** 123801

Lucarini V and Bódai T 2020 Global stability properties of the climate: Melancholia states, invariant measures and phase transitions *Nonlinearity* **33** R59–R92

Rahmstorf S 1994 Rapid climate transitions in a coupled ocean-atmosphere model *Nature* **372** 82–84

Rahmstorf S 1995 Multiple Convection Patterns and Thermohaline Flow in an Idealized OGCM *J. Clim.* **8** 3028–39

Rahmstorf S 1996 On the freshwater forcing and transport of the Atlantic thermohaline circulation *Clim. Dyn.* **12** 799–811

Rahmstorf S 2024 Is the Atlantic overturning circulation approaching a tipping point? *Oceanography* **37** 16–29

Sgubin G, Swingedouw D, Drijfhout S, Mary Y and Bennabi A 2017 Abrupt cooling over the North Atlantic in modern climate models *Nat. Commun.* **8** 14375

Stommel H 1961 Thermohaline convection with two stable regimes of flow *Tellus* **13** 224–30

Swingedouw D, Bily A, Esquerdo C, Borchert L F, Sgubin G, Mignot J and Menary M 2021 On the risk of abrupt changes in the North Atlantic subpolar gyre in CMIP6 models *Ann. New York Acad. Sci.* **1504** 187–201

Thies J, Wubs F and Dijkstra H A 2009 Bifurcation analysis of 3D ocean flows using a parallel fully-implicit ocean model *Ocean Model.* **30** 287–97

Trenberth K E, Olson J G and Large W G (1989) A global ocean wind stress climatology based on ECMWF analyses, *Technical Report* (NCAR) (available at: https://opensky.ucar.edu/islandora/object/technotes%3A107)

van Westen R M, Kliphuis M and Dijkstra H A 2024 Physics-based early warning signal shows that amoc is on tipping course *Sci. Adv.* **10** eadk1189

Van Westen R M, Kliphuis M and Dijkstra H A 2025 Collapse of the Atlantic meridional overturning circulation in a strongly eddying ocean-only model *Geophys. Res. Lett.* **52** e2024GL114532

van Westen R M, Vanderborght E and Dijkstra H A 2025 A saddle-node bifurcation is causing the AMOC collapse in the community earth system model *Earth Syst. Dyn.* **16** 2063–85

Vanderborght E, van Westen R M and Dijkstra H A 2025 Feedback processes causing an AMOC collapse in the community earth system model *J. Clim.* **38** 5083–102

Vellinga M 1998 Multiple equilibria of the thermohaline circulation as a side effect of convective adjustment *J. Phys. Oceanogr.* **28** 305–19

Welander P 1982 A simple heat-salt oscillator *Dyn. Atmos. Oceans* **6** 233–42

Wubs F W and Dijkstra H A 2023 *Bifurcation Analysis of Fluid Flows* (Cambridge University Press) (https://doi.org/10.1017/9781108863148)